The Thesis committee for Paul Daniel Schnase Certifies that this is the approved version of the following thesis:

Floquet Topological Transitions in Extended Kane-Mele Models with Disorder

SUPERVISING COMMITTEE:

Gregory Fiete, Supervisor

Allen MacDonald

Floquet Topological Transitions in Extended Kane-Mele Models with Disorder

by

Paul Daniel Schnase

Thesis

Presented to the Faculty of the Graduate School

of the University of Texas at Austin

in Partial Fulfillment

of the Requirements

for the Degree of

Master of Arts

The University of Texas at Austin

December 2018

Floquet Topological Transitions in Extended Kane-Mele Models with Disorder

by

Paul Daniel Schnase, MA

The University of Texas at Austin, 2018

SUPERVISOR: Gregory Fiete

In this thesis we use Floquet theory to theoretically study the influence of circularly polarized light on disordered two-dimensional models exhibiting topological transitions. We find circularly polarized light can induce a topological transition in extended Kane-Mele models that include additional hopping terms and on-site disorder. The topological transitions are understood from the Floquet-Bloch band structure of the clean system at high symmetry points in the first Brillouin zone. The light modifies the equilibrium band structure of the clean system in such a way that the smallest gap in the Brillouin zone can be shifted from the M points to the $K(K')$ points, the Γ point, or even other lower symmetry points. The movement of the minimal gap point through the Brillouin zone as a function of laser parameters is explained in the high frequency regime through the Magnus expansion. In the disordered model, we compute the Bott index to reveal topological phases and transitions. The disorder can induce transitions from topologically non-trivial states to trivial states or vice versa, both examples of Floquet topological Anderson transitions. As a result of the movement of the minimal gap point through the Brillouin zone as a function of laser parameters, the nature of the topological phases and transitions is laser-parameter dependent–a contrasting behavior to the Kane-Mele model.

Contents

1

Introduction

The Kane-Mele model is an example of a lattice model used to understand crystalline solids, an important topic in condensed matter physics. In particular, the Kane-Mele model uses a honeycomb lattice, like that of graphene. This thesis explores several variations on the Kane-Mele model, which represents electrons as being at the lattice sites. The electrons can hop from one site to nearest neighbor sites and to second-nearest neighbor sites. This thesis extends that model to allow hopping to third-nearest neighbor sites or to pair the atoms, with each atom bonded to one of its nearest neighbors with different strength from its other two neighbors. The model is also extended by shining a laser on the lattice and by introducing on-site disorder. In each of these cases, we study whether the model produces a topological insulator or a trivial insulator.

On a honeycomb lattice (see Figure 2.1), the electrons can move from one lattice site to an adjacent lattice site with a certain amplitude, represented by the parameter t_1. Determining

the best value of this and other parameters to represent a real material may be complicated, but for the purposes of this thesis, we set $t_1 = 1$. This choice simply sets the energy scale of the calculations, so is done without loss of generality.

The electrons are also allowed to move to the second-nearest neighbor sites. Due to spin-orbit coupling, the second-nearest neighbor terms in the Hamiltonian are imaginary, so are antisymmetric. The strength of the second-nearest neighbor interaction is denoted by λ_{soc}. The nearest neighbor hopping and the second-nearest neighbor spin-orbit coupling terms form the Kane-Mele model, which this thesis extends in several ways.

The first extension is the generalized Kane-Mele model (GKM), which allows hopping between third-nearest neighbors. Third-nearest neighbor hopping is symmetric like first-nearest neighbor hopping and its strength is determined by the parameter t_3. The second extension is the dimerized Kane-Mele model (DKM), in which the two atoms within the same unit cell of the honeycomb lattice have a different hopping parameter with each other than with their nearest neighbors in other unit cells. Sec. 2.2 has a more mathematical description of the GKM and DKM models.

The GKM and DKM models are further extended with the addition of on-site disorder and the application of a laser.

Disorder is represented in the system by adding a random number to each of the diagonal entries of the Hamiltonian matrix. Essentially, disorder causes electrons to prefer some lattice sites over others. Random numbers are chosen from a uniform distribution in the range from $-U_{dis}/2$ to $U_{dis}/2$, where U_{dis} is another parameter. The disorder in the system means that it

is no longer periodic in space, which necessitates that calculations be done in real-space with a finite sample size. Periodic boundary conditions are then imposed on that finite sample.

The laser, with amplitude A_0 and frequency Ω, makes the Hamiltonian periodic in time, thus Floquet's theorem applies to the system. Floquet's theorem states that periodicity in time in the Hamiltonian imposes periodicity in energy, so the band structure becomes periodic in quasienergy with period Ω. If the amplitude of the laser is low, states from one periodic image are only slightly coupled to states in other periodic images. Two frequencies are studied, the off-resonance case where Ω is greater than the bandwidth and the on-resonance case where Ω is less than the bandwidth. Because the Floquet copies substantially increase the size of the Hamiltonian matrix, it is necessary to limit the number of Floquet copies considered when doing numerical calculations. The influence of the laser also changes the shape of the bands, as seen in Figure 4.2.

A method is described to calculate the topological invariant, the Bott index. This invariant is used to determine if the system is a topological insulator or a trivial insulator. The Bott index is equivalent to the Chern number in cases when both apply. The term Chern number is used in clean systems, without disorder, when there is translational symmetry. The term Bott index is used when the system has disorder, which destroys the translational symmetry. The topological invariant must take an integer value for a given system. If the system is topologically insulating with symmetry-protected conducting states on the surface, the invariant is odd. If the system is topologically trivial without such surface states, the invariant is even.

Finally, the results of those calculations are presented, including band structures, the size of the band gap of the system, and phase diagrams of the Bott index.

The extensions of the Kane-Mele model studied in this thesis exhibit different topological phases depending on the values of the parameters and the iteration of the disorder. In systems without disorder, it is possible to calculate the invariant just once for a set of parameters, and phase transitions are sharp. For systems with disorder, the Bott index depends on the exact configuration of the disorder. The Bott index must be calculated and averaged across a representative sample of disorder iterations. Each iteration has an integer Bott index, but different iterations may disagree, so the phase transitions are blurred. In the limit of infinite system size, the transitions would become sharp, but, as demonstrated by Fig 4.6, choosing a larger size that is still calculable in a reasonable amount of time would not meaningfully change the results.

2

Model

2.1 Introduction

Research on topological band insulators has seen dramatic progress in the past decade.[1–4] The phenomenology is even richer when inter-particle interactions are taken into account and fractionalized phases result. [5–9] Starting from a non-interacting band structure, the Coulomb interaction can induce a topological transition.[10–12] For example, in the two-dimensional honeycomb lattice, the Dirac points are stable to weak Coulomb interaction, while the bulk gap will open at a finite critical Coulomb interaction.[13–15] In the kagome lattice, there is a flat band and a quadratic band touching point which is perturbatively unstable to the Coulomb interaction.[10, 16] Recently, an active direction of research has been to study the topological transition by periodically driving a non-interacting system to a non-equilibrium state, called a Floquet topological insulator.[17] A periodic drive can be realized in a cold atom system with

---

Portions of this chapter are based on an article published as L. Du, P. D. Schnase, A. D. Barr, A. R. Barr, and G. A. Fiete, Phys. Rev. B 98, 054203 2018). All authors contributed to the original article.

an optical lattice potential generated by changing the laser field,[18, 19] or in the solid state by illumination with a monochromatic laser field. [20–39]

In equilibrium, topological insulators induced by Anderson (on-site) disorder have been well studied in the past decade. [40–51] Within the Born approximation, Anderson disorder will induce a negative correction to the mass and chemical potential, which in turn may induce a topological transition.[41] Song *et al.*[52] studied the effect of different types of disorder on the topological transition in the Haldane model where a Dirac point is situated at the K, K' points. Their study shows that on-site disorder and bond disorder have different effects on the topological transition. Bond disorder tends to prohibit the system from undergoing a phase transition to a topological Anderson insulator, contrary to the effect of Anderson disorder. When the Kane-Mele model[53, 54] is generalized to include third-neighbor hopping, or dimerized first-neighbor hopping terms along the z direction, the linear crossing can shift from a K, K' point to an M point.[55] At the M point, the bond and on-site disorder have the same effect on the mass renormalization, and both enhance the topological state in the weak disorder limit.[55] Hung *et al.*[55] studied the generalized Kane-Mele (GKM) model and dimerized Kane-Mele (DKM) model (described in this thesis in Sec. 2.2). They found that low and intermediate levels of disorder tend to stabilize the topological phase for both models. Further, taking the Coulomb interaction into account tends to destabilize the topological phase in the dimerized Kane-Mele model, but stabilize the topological phase in the GKM model. Hence the GKM and DKM provide contrasting behavior to each other, and also to the more heavily studied Kane-Mele model, thus illustrating the phenomenological richness of topological phases and transitions under different conditions.

To summarize, the location of the Dirac point in momentum space in a clean (disorder-free) system is crucial to determining the effect of bond or on-site disorder. In this thesis, we show that starting from a fixed equilibrium model Hamiltonian, periodically driving the system out-of-equilibrium via a laser can shift the Dirac point between different high symmetry points, for example, from an M to a K or a Γ point. These shifts are computed in detail, and provide a platform to study differences in the effects of bond and on-site disorder in the presence of a laser field. Out-of-equilibrium, a disorder-induced transition between topologically trivial and nontrivial states is characterized by the disorder-averaged Bott index.[56] Prior non-equilibrium work studied the honeycomb lattice with staggered on-site A-B sub-lattice potentials in the presence of disorder.[57, 58]

In this thesis, we focus on laser- and disorder-induced topological transitions. Before turning to the disorder-induced Floquet topological phase transition in the GKM and DKM models, we first study the Floquet-Bloch band structure where a gap closing and reopening process is observed. The effect of disorder on the clean Floquet system is studied and the results qualitatively explained considering the energy scales of the system gap size and the total bandwidth.

The organization in this thesis is as follows. In Sec.2.2, we describe the generalized Kane-Mele and dimerized Kane-Mele models. Sec.3.1 introduces Floquet theory. Sec. 3.2 provides details on the numerical calculations performed. Sec.4.1 covers the Floquet topological transition, the Floquet-Bloch band structure, and the related low-energy theory. In Sec.4.2, we study the topological transition in the generalized and dimerized Kane-Mele models subject to both laser illumination and on-site disorder. Sec. 4.3 examines the topological invariant when the laser is on-resonant (i.e. the frequency of the laser is such that the energy of a photon is less

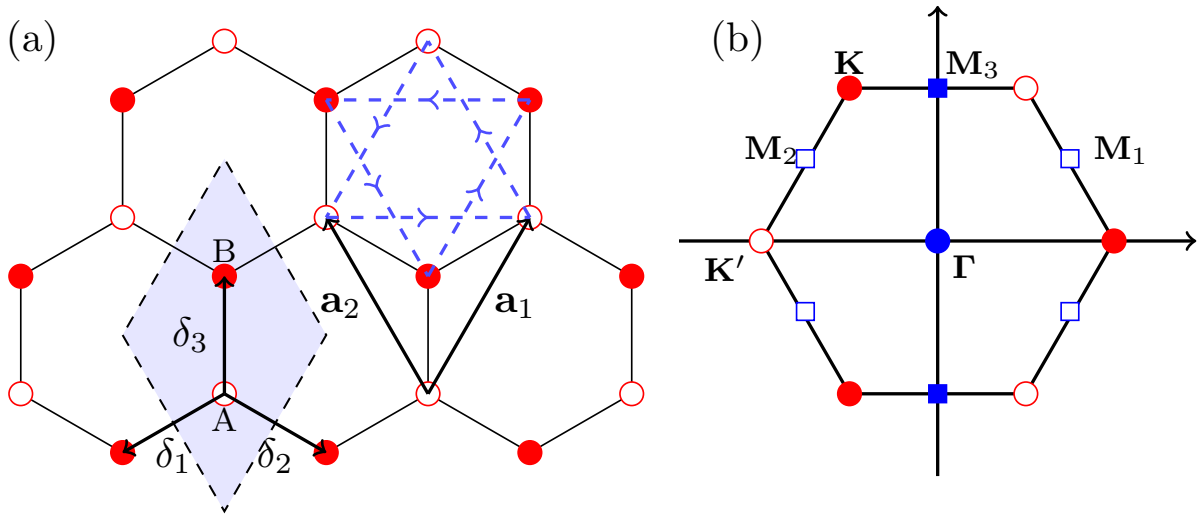

FIGURE 2.1: (Color online) (a) Honeycomb lattice with two sub-lattices in one unit cell (shaded area), labeled A (open circles) and B (filled circles). Three nearest-neighbor unit vectors are $\delta_1 = (-\sqrt{3}/2, -1/2)a$, $\delta_2 = (\sqrt{3}/2, -1/2)a$, $\delta_3 = (0, 1)a$, with a the nearest-neighbor distance. Lattice translational vectors are labeled as $\mathbf{a}_1 = \delta_3 - \delta_1 = (\sqrt{3}/2, 3/2)a, \mathbf{a}_2 = \delta_3 - \delta_2 = (-\sqrt{3}/2, 3/2)a$. The blue dashed lines represent the imaginary second-neighbor hopping (spin-orbit coupling) and the arrow directions represent positive signs. (b) First Brillouin zone of the underlying triangular Bravais lattice with reciprocal lattice vector $\mathbf{b}_1 = (\sqrt{3}, 1)2\pi/(3a)$ and $\mathbf{b}_2 = (-\sqrt{3}, 1)2\pi/(3a)$. High symmetry points are $\mathbf{K} = (-2\pi/\sqrt{3}, 2\pi)/(3a)$, $\mathbf{K}' = (-4\pi/\sqrt{3}, 0)/(3a)$ and time reversal invariant momenta $\mathbf{M}_{1,2} = (\pm\sqrt{3}\pi, \pi)/(3a)$, $\mathbf{M}_3 = (0, 2\pi)/(3a)$. All filled circles are equivalent to $\mathbf{K}$ and all open circles are equivalent to $\mathbf{K}'$. The Floquet quasi-band structure is plotted along the momentum path $K' - \Gamma - M_3 - K - M_2 - K'$ in the first Brillouin zone.

than the bandwidth of the equilibrium system). Finally, in Sec.4.4, we summarize our main conclusions.

2.2 Model Hamiltonian

We study both the generalized Kane-Mele (GKM) tight-binding Hamiltonian with third-nearest neighbor hopping terms and the dimerized Kane-Mele (DKM) model with dimerized hopping

parameter in the vertical direction on the honeycomb lattice (Fig.2.1(a)). The GKM Hamiltonian in real-space is given by, 2.1

$$H^{\sigma}_{\mathrm{GKM}} = -t_1 \sum_{\langle ij\rangle} c_i^{\dagger} c_j + i\lambda_{\mathrm{soc}} \sum_{\langle\langle ij\rangle\rangle} \sigma v_{ij} c_i^{\dagger} c_j - t_3 \sum_{\langle\langle\langle ij\rangle\rangle\rangle} c_i^{\dagger} c_j \tag{2.1}$$

where $t_1(t_3)$ is the isotropic hopping integral between first- (third-) nearest neighbors, $c_i^{\dagger}$ (c_j) creates (annihilates) an electron with spin σ on site i (j) of the honeycomb lattice (the spin subindex is omitted for simplicity), and $\langle ij\rangle$ limits the summation to nearest neighbors, $\langle\langle ij\rangle\rangle$ and $\langle\langle\langle ij\rangle\rangle\rangle$ limit the summation to second- and third-nearest neighbors, respectively. Here λ_{soc} is the spin-orbit coupling strength, $\sigma = 1(-1)$ for a spin-$\uparrow$ ($\downarrow$) sector Hamiltonian, $v_{ij} = 1$ for the counter-clockwise hopping shown in Fig.2.1(a) with dashed arrow lines, and $v_{ij} = -1$ for clockwise hopping. In Eq.(2.1) only the spin-σ part of the Hamiltonian is written explicitly. The Hamiltonian with opposite spin-$\bar{\sigma}$ is the time-reversal of $H^{\sigma}_{\mathrm{GKM}}$.

The DKM Hamiltonian in real-space is given by,

$$H^{\sigma}_{\mathrm{DKM}} = \sum_i (-t_1(c_i^{\dagger} c_{i+\delta_1} + c_i^{\dagger} c_{i+\delta_2}) - t_d c_i^{\dagger} c_{i+\delta_3} + h.c.) + i\lambda_{\mathrm{soc}} \sum_{\langle\langle ij\rangle\rangle} \sigma v_{ij} c_i^{\dagger} c_j, \tag{2.2}$$

where t_d is the nearest-neighbor hopping parameter along the vertical direction (δ_3 in Fig.2.1(a)). For conciseness, we write the Hamiltonian with a general form,

$$\begin{aligned} H^{\sigma} = & \sum_i -t_1(c_i^{\dagger} c_{i+\delta_1} + c_i^{\dagger} c_{i+\delta_2}) - t_d c_i^{\dagger} c_{i+\delta_3} + h.c. \\ & + i\lambda_{\mathrm{soc}} \sum_{\langle\langle ij\rangle\rangle} \sigma v_{ij} c_i^{\dagger} c_j - t_3 \sum_{\langle\langle\langle ij\rangle\rangle\rangle} c_i^{\dagger} c_j. \end{aligned} \tag{2.3}$$

In this form, we have the GKM model when $t_d = t_1$ and we have the DKM when $t_3 = 0.0, t_d \neq t_1$. Fourier transforming the Hamiltonian in Eq.(2.3) to momentum space, we obtain $H^\sigma = \sum_{\mathbf{k}} \psi^\dagger_{\mathbf{k}} H_{\mathbf{k}} \psi_{\mathbf{k}}$ with $\psi_{\mathbf{k}} = (c_{\mathbf{k}A}, c_{\mathbf{k}B})^T$, where $c_{\mathbf{k}A}$ and $c_{\mathbf{k}B}$ define annihilation operators on the two basis sites in the unit cell shown in Fig.2.1(a). In the following, we focus on the spin-$\uparrow$ Hamiltonian only,

$$H_{\mathbf{k}\uparrow} = \begin{pmatrix} 0 & -f_1(\mathbf{k}) - t_3 f_3(\mathbf{k}) \\ -f_1^*(\mathbf{k}) - t_3 f_3^*(\mathbf{k}) & 0 \end{pmatrix} + \begin{pmatrix} -\lambda_{soc} g(\mathbf{k}) & 0 \\ 0 & \lambda_{soc} g(\mathbf{k}) \end{pmatrix}, \tag{2.4}$$

where

$$g(\mathbf{k}) = -2\sin(\mathbf{k}\cdot\mathbf{a}_1) + 2\sin(\mathbf{k}\cdot\mathbf{a}_2) + 2\sin(\mathbf{k}\cdot\mathbf{a}_1 - \mathbf{k}\cdot\mathbf{a}_2)$$

$$f_1(\mathbf{k}) = t_d + t_1 e^{-i\mathbf{k}\cdot\mathbf{a}_1} + t_1 e^{-i\mathbf{k}\cdot\mathbf{a}_2} \tag{2.5}$$

$$f_3(\mathbf{k}) = e^{-i\mathbf{k}\cdot(\mathbf{a}_1+\mathbf{a}_2)} + 2\cos(\mathbf{k}\cdot\mathbf{a}_1 - \mathbf{k}\cdot\mathbf{a}_2).$$

The lattice vectors, $\mathbf{a}_1$ and $\mathbf{a}_2$, are defined in Fig.2.1. For the GKM model, the gap opened at the $\mathbf{\Gamma}$ point is $|6(t_1 + t_3)|$; at the $\mathbf{K}$ and $\mathbf{K}'$ points, the gaps are $|6\sqrt{3}t_2|$; and the gaps at $\mathbf{M}_{1,2,3}$ points are $2|t_1 - 3t_3|$. In this thesis, we fix $t_1 = 1.0, t_2 = -0.3$ to make sure the equilibrium system band gap is situated at the M points. When Eq.(2.3) is exposed to a normally incident

laser field, the time-dependent Hamiltonian can be expressed as

$$
\begin{aligned}
H(t) = & \sum_{i} \left[-t_1 c_i^{\dagger} c_{i+\delta_1} - t_1 c_i^{\dagger} c_{i+\delta_2} - t_d c_i^{\dagger} c_{i+\delta_3} \right] e^{-iA_{ij}(t)} \\
& - t_3 \sum_{\langle\langle\langle ij \rangle\rangle\rangle} c_i^{\dagger} c_j e^{-iA_{ij}(t)} + h.c. \\
& + i\lambda_{soc} \sum_{\langle\langle ij \rangle\rangle} \sigma v_{ij} c_i^{\dagger} c_j e^{-iA_{ij}(t)} \ ,
\end{aligned} \tag{2.6}
$$

where $A_{ij}(t) = \mathbf{A}(t) \cdot (\mathbf{R}_j - \mathbf{R}_i)$, $\mathbf{A}(t) = A_0[\sin(\Omega t), \cos(\Omega t)]$ is the vector potential with A_0 the amplitude and Ω the frequency of the laser. The relation $\mathbf{R}_j = \mathbf{R}_i + \delta_i$ with $i = 1, 2, 3$ for each term holds. In Eq.(2.6), we set Planck's constant $\hbar = 1$, the speed of light $c = 1$, the charge of the electron $e = 1$, and adopt the Coulomb gauge by setting the scalar potential $\phi = 0$. We ignore the tiny effect of the magnetic field of the laser field. The units of energy are expressed in terms of the nearest-neighbor hopping amplitude t_1, for $t_1 = 1$,

$$
H_{\mathbf{k}\uparrow}(t) = \begin{pmatrix} 0 & -f_1(\mathbf{k}, t) \\ -f_1^*(\mathbf{k}, t) & 0 \end{pmatrix} + \begin{pmatrix} -\lambda_{soc} g(\mathbf{k}, t) & -t_3 f_3(\mathbf{k}, t) \\ -t_3 f_3^*(\mathbf{k}, t) & \lambda_{soc} g(\mathbf{k}, t) \end{pmatrix}, \tag{2.7}
$$

where

$$
\begin{aligned}
g(\mathbf{k}, t) \equiv & \, i e^{i\mathbf{k}\cdot\mathbf{a}_1 - i\mathbf{A}(t)\cdot\mathbf{a}_1} - i e^{-i\mathbf{k}\cdot\mathbf{a}_1 + i\mathbf{A}(t)\cdot\mathbf{a}_1} \\
& - i e^{i\mathbf{k}\cdot\mathbf{a}_2 - i\mathbf{A}(t)\cdot\mathbf{a}_2} + i e^{-i\mathbf{k}\cdot\mathbf{a}_2 + i\mathbf{A}(t)\cdot\mathbf{a}_2} \\
& - i e^{i\mathbf{k}\cdot\mathbf{a}_3 - i\mathbf{A}(t)\cdot\mathbf{a}_3} + i e^{-i\mathbf{k}\cdot\mathbf{a}_3 + i\mathbf{A}(t)\cdot\mathbf{a}_3},
\end{aligned} \tag{2.8}
$$

$$f_1(\mathbf{k},t) = t_d e^{-i\mathbf{A}(t)\cdot\delta_3} + t_1 e^{-i\mathbf{k}\cdot\mathbf{a}_1} e^{-i\mathbf{A}(t)\cdot\delta_1} + t_1 e^{-i\mathbf{k}\cdot\mathbf{a}_2} e^{-i\mathbf{A}(t)\cdot\delta_2}, \tag{2.9}$$

and

$$f_3(\mathbf{k},t) = e^{-i\mathbf{k}\cdot(\mathbf{a}_1+\mathbf{a}_2)} e^{i\mathbf{A}(t)\cdot 2\delta_3} + e^{i\mathbf{k}\cdot\mathbf{a}_3} e^{-i\mathbf{A}(t)\cdot(\mathbf{a}_1+\delta_2)} + e^{-i\mathbf{k}\cdot\mathbf{a}_3} e^{-i\mathbf{A}(t)\cdot(\mathbf{a}_2+\delta_1)}. \tag{2.10}$$

The on-site disorder is added to the system through the addition of

$$H_{dis} = \sum_i U^i_{dis} c^\dagger_i c_i, \tag{2.11}$$

where U^i_{dis} is uniformly distributed in the range $[-U_{dis}/2, U_{dis}/2]$.

3

Floquet Theory and Bott Index

3.1 Floquet Theory

In this thesis, we illuminate the system with monochromatic (single frequency) light, which renders the Hamiltonian time-periodic: $H(t) = H(t+T)$ where T is the period of the laser drive. Hence, Floquet's theorem is applicable. The Floquet eigenfunction in real space for the time-periodic Hamiltonian can be expressed as,

$$|\Psi_\alpha(t)\rangle = e^{-i\epsilon_\alpha t}|\phi_\alpha(t)\rangle, \tag{3.1}$$

where $|\phi_\alpha(t)\rangle = |\phi_\alpha(t+T)\rangle$ are the Floquet quasi-modes and ϵ_α is the corresponding quasi-energy for band α. Substituting the wave function above into the time-dependent Schrödinger

---

Portions of this chapter are based on an article published as L. Du, P. D. Schnase, A. D. Barr, A. R. Barr, and G. A. Fiete, Phys. Rev. B 98, 054203 2018). All authors contributed to the original article.

equation, and defining the Floquet Hamiltonian operator as $\mathcal{H}(t) = H(t) - i\partial/\partial t$, one finds

$$\mathcal{H}(t)|\phi_{k\alpha}(t)\rangle = \epsilon_\alpha|\phi_\alpha(t)\rangle. \tag{3.2}$$

Here we restrict the quasienergy to be in the first Floquet zone, *i.e.*, $-\Omega/2 < \epsilon_\alpha < \Omega/2$. (Note that we have made use of a spin-independent coupling to the laser field so that all bands are 2-fold degenerate. Henceforth, we suppress the spin degeneracy.) Solving for the Floquet states in Fourier space,

$$|\phi_\alpha(t)\rangle = \sum_m e^{im\Omega t}|\tilde{\phi}^m_\alpha\rangle, \tag{3.3}$$

where $m = 0, \pm1, \pm2, \cdots$ and $|\tilde{\phi}^m_{k\alpha}\rangle$ is a real space vector which obeys,

$$\sum_m (H_{nm} + m\Omega\delta_{nm})|\tilde{\phi}^m_\alpha\rangle = \epsilon_\alpha|\tilde{\phi}^m_\alpha\rangle, \tag{3.4}$$

with matrix elements of the Floquet Hamiltonian written as,

$$H_{nm} = \frac{1}{T}\int_0^T dt e^{-i(n-m)\Omega t}H(t). \tag{3.5}$$

Here m and n are integers ranging from $-\infty$ to ∞. Thus, the Floquet matrix is an infinite-dimensional time-independent matrix. In this thesis, we consider the laser frequency to be comparable to or larger than the bandwidth of the system, so a truncation of the components to be in $m, n = -2, -1, 0, 1, 2$ is a good approximation. We have numerically verified that including a larger range of m, n has a very small numerical impact on our results.

For circularly polarized light with vector potential $\mathbf{A}(t) = A_0[\sin(\Omega t), \cos(\Omega t)]$, the matrix elements of the Floquet-Bloch Hamiltonian are

$$H_{nm}^{ij} = \frac{1}{T}\int_0^T dt e^{-i(n-m)\Omega t} \exp[-iA_{ij}(t)]H^{ij}, \tag{3.6}$$

from the expression with the general form,

$$f_{nm} = \frac{1}{T}\int_0^T dt e^{-i(n-m)\Omega t} \exp[-i\mathbf{A}(t)\cdot\mathbf{d}]. \tag{3.7}$$

Here we used $\mathbf{d} = \mathbf{R}_j - \mathbf{R}_i$, and define $d^x/|\mathbf{d}| = \cos\theta$, $d^y/|\mathbf{d}| = \sin\theta$. For nearest-neighbor hopping terms, $|\mathbf{d}| = 1$, $\theta = \pm 5\pi/6, \pm\pi/6, \mp\pi/2$. Substituting the vector potential into the above equation gives,

$$\frac{1}{T}\int_0^T dt e^{-i(n-m)\Omega t} \exp[-iA_0(d^x \sin\Omega t + d^y \cos\Omega t)] = \quad \mathcal{J}_{m-n}(A_0|\mathbf{d}|)\exp[i(n-m)\theta], \tag{3.8}$$

where $\mathcal{J}_n(x)$ is the Bessel function of first kind. In this thesis,we used two equivalent expressions for the topological invariant, the Chern number and the Bott index[36, 56, 59]. Here we use different expressions to show we used different methods to calculate the topological invariant. For the Floquet system with translational symmetry, we used Fukui's method [59] to calculate the Chern number. For the Floquet system with random on-site disorder, we calculate the Bott index using the C^* theory.[56]

3.2 Calculating the Bott Index

To find the Bott index numerically, we first define two unitary diagonal matrices:

$$U_{Xnn} = \exp(2\pi i x_n / L_x) \tag{3.9}$$

$$U_{Ynn} = \exp(2\pi i y_n / L_y)$$

where x_n, y_n, L_x, and L_y are numbers defined so that atom n is located at the point $x_n\mathbf{a}_1 + y_n\mathbf{a}_2$ and so that L_x, and L_y are the number of unit cells in the $\mathbf{a}_1$ and $\mathbf{a}_2$ directions. Thus if you put one of the particles at the origin, then half of the particles (one per unit cell) will have integer values of x_n and y_n, and moving by $L_x\mathbf{a}_1$ or $L_x\mathbf{a}_2$ moves from one point to its corresponding point in an adjacent periodic image. In the extended Floquet Hilbert space,

$$U_X^F = \begin{pmatrix} U_X & & 0 \\ & \ddots & \\ 0 & & U_X \end{pmatrix}, \tag{3.10}$$

with U_Y^F defined analogously. This is still a diagonal, unitary matrix, and the number of copies of U_X or U_Y is equal to the number of Floquet copies being considered in the calculation. These matrices contain information on the geometry of the system (i.e. the locations of the atoms).

The Hamiltonian of the system is similar to Eq.2.3, but must account for the disorder and the influence of the laser. Including the disorder,

$$H_{jk} = \sum_j u_j - t_1(c_j^\dagger c_{j+\delta_1} + c_j^\dagger c_{j+\delta_2}) - t_d c_j^\dagger c_{j+\delta_3} + h.c. \\ + i\lambda_{soc} \sum_{\langle\langle jk \rangle\rangle} v_{jk} c_j^\dagger c_k - t_3 \sum_{\langle\langle\langle jk \rangle\rangle\rangle} c_j^\dagger c_k, \tag{3.11}$$

where u_j is a random perturbation on site j with a strength in the range $[-U_{dis}/2, U_{dis}/2]$ using a uniform distribution. Copies of this Hamiltonian become blocks in the Floquet Hamiltonian, but the elements are also changed due to the laser.

$$H_{nm}^{jk} = H_{jk} \mathcal{J}_{m-n}(A_0 |\mathbf{d_{jk}}|) \exp[i(n-m)\theta_{jk}], \tag{3.12}$$

where m and n are indices for the blocks of the matrix, while j and k are indices within a block of the matrix, and $|\mathbf{d_{jk}}|$ and θ_{jk} are the distance and direction, respectively, from site j to site k. Note that a single site should have the same random perturbation across all Floquet copies

Next, choose an appropriate set of eigenvectors, $|\epsilon\rangle$, of the Hamiltonian. This thesis calculates the Bott index of all states with quasi-energy $\epsilon < 0$ in the truncated Floquet space. The next matrix to define is the projector onto the subspace of those eigenvectors.

$$P = \sum_{\epsilon<0} |\epsilon\rangle\langle\epsilon| \tag{3.13}$$

This contains information about which sites the electrons can hop between, as well as the values of the parameters (i.e. t_1, λ_{soc}, A_0, etc) and the iteration of disorder.

Combine these matrices to form the projected unitary matrices,

$$\tilde{U}_Y^F = PU_X^F P \qquad\qquad \tilde{U}_X^F = PU_Y^F P \tag{3.14}$$

The Bott index of the chosen states is then

$$C_b = \frac{1}{2\pi}\mathrm{Im}\left[\mathrm{Tr}\left(\log\left(\tilde{U}_Y^F \tilde{U}_X^F \tilde{U}_Y^{F\dagger} \tilde{U}_X^{F\dagger}\right)\right)\right] \tag{3.15}$$

or, equivalently,

$$C_b = \frac{1}{2\pi}\mathrm{Im}\left[\sum_{i\ s.t.\ \lambda_i \neq 0} \log\left(\lambda_i\right)\right] \tag{3.16}$$

where λ_i are the nonzero eigenvalues of $\tilde{U}_Y^F \tilde{U}_X^F \tilde{U}_Y^{F\dagger} \tilde{U}_X^{F\dagger}$

The cluster size, which is the number of unit cells along a_1 and a_2, is 24 by 24, giving 1152 sites (two sites per unit cell). The number of Floquet copies is 5.

4

Results

4.1 Spin Chern number for the disorder-free system

4.1.1 Spin Chern number and Floquet band structure

In Fig.4.1, we plot the spin Chern number as a function of laser intensity for different third-neighbor hopping parameters $t_3 = 0.0, 0.2, 0.4$ in the generalized Kane-Mele model [Eq.(2.1)] and different dimerized hopping parameters $t_d = 1.5, 2.0, 2.5$ in the dimerized Kane-Mele model [Eq.(2.2)].

In the equilibrium case (absent the laser, i.e. $A_0 = 0$) of the GKM model, the system gap is determined by the bands at the $M_{1,2,3}$ points. By tuning the third-neighbor hopping parameter, the transition from topologically non-trivial ($\mathcal{C} = -1$) to topologically trivial ($\mathcal{C} = 2$) occurs at the critical value of $t_3 = 1/3$, where the gap at $M_{1,2,3}$ (C_3 rotational symmetry is conserved)

Portions of this chapter are based on an article published as L. Du, P. D. Schnase, A. D. Barr, A. R. Barr, and G. A. Fiete, Phys. Rev. B 98, 054203 2018). All authors contributed to the original article.

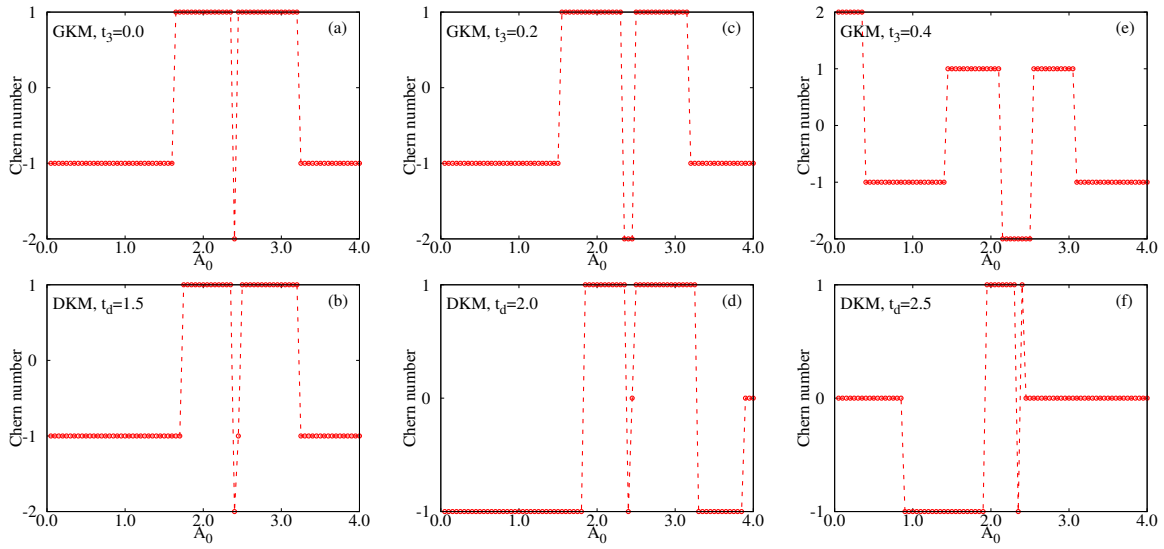

FIGURE 4.1: (Color online) The spin Chern number as a function of laser amplitude A_0 for the generalized Kane-Mele model (top row, Eq. (2.1)) with $t_3 = 0.0$ (a), $t_3 = 0.20$ (c), $t_3 = 0.40$ (e) and the dimerized Kane-Mele model (bottom row, Eq. (2.2)) with $t_d = 1.5$ (b), $t_d = 2.0$ (d), $t_d = 2.50$ (f). The remaining parameters are nearest-neighbor hopping $t_1 = 1.0$, spin-orbit coupling $\lambda_{soc} = 0.3$, and laser frequency $\Omega = 10.0$. All the calculations are done with 2500 **k**-points in the first Brillouin zone and 9 Floquet copies.

closes and reopens, inducing a ± 3 change of spin Chern number. This is the starting point of the non-equilibrium study shown in Fig.4.1(a),(c),(e).

In the DKM model, by comparison, the system gap is determined by the bands at the M_3 point. By tuning the dimerized nearest-neighbor hopping, the transition from topologically non-trivial ($\mathcal{C} = -1$) to topologically trivial ($\mathcal{C} = 0$) occurs. Increasing the dimerized hopping parameter will close the gap at the M_3 point (C_3 rotational symmetry is broken), and reopen the gap at the critical value $t_d = 2.0$, inducing a change of Chern number $\Delta\mathcal{C} = \pm 1$. This is the starting point of the non-equilibrium study in Fig.4.1 (b),(d),(f).

The spin Chern number shows complicated structure for both the GKM and DKM models when illuminated with a laser. Since Fig.4.1(a),(b),(c),(d) have very similar structure (due to the same starting topological phase as the Kane-Mele model), our analysis of the topological

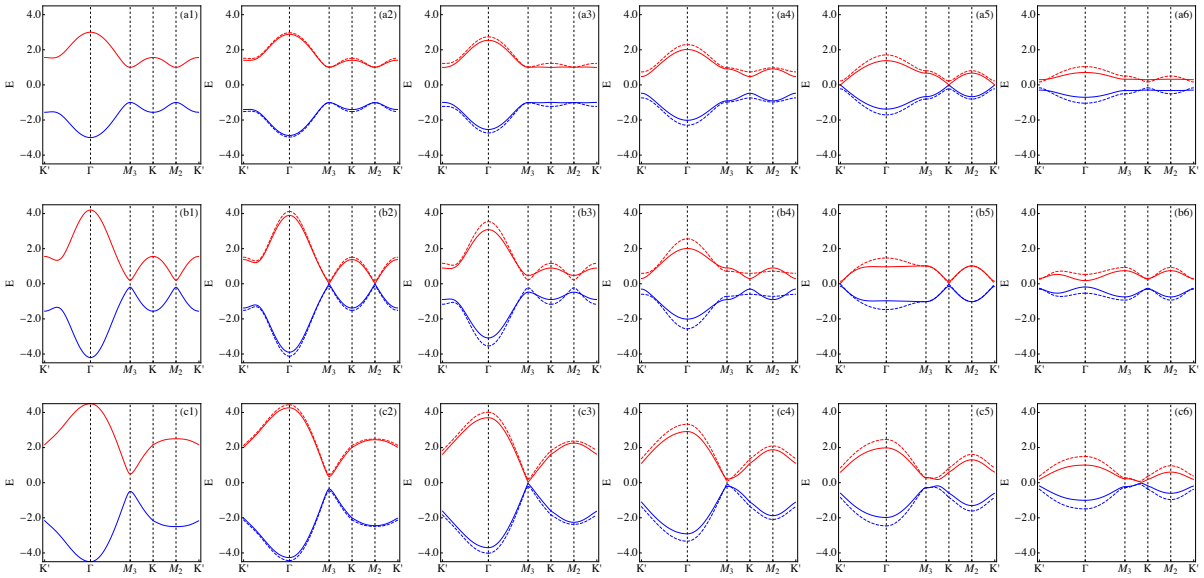

FIGURE 4.2: (Color online) (a, top row) The Floquet-Bloch band structure of the Kane-Mele model [Eq. (2.1)] with (a1) $A_0 = 0$, (a2) $A_0 = 0.2$ and 0.4, (a3) $A_0 = 0.6$ and 0.8, (a4) $A_0 = 1$ and 1.2, (a5) $A_0 = 1.4$ and 1.6, and (a6) $A_0 = 1.8$ and 2.0. (b, middle row) The Floquet-Bloch band structure of the generalized Kane-Mele model [Eq. (2.1)] with (b1) $A_0 = 0$, (b2) $A_0 = 0.2$ and 0.4, (b3) $A_0 = 0.6$ and 0.8, (b4) $A_0 = 1$ and 1.2, (b5) $A_0 = 1.4$ and 1.6, and (b6) $A_0 = 1.8$ and 2.0. (c, bottom row) The Floquet-Bloch band structure of the dimerized Kane-Mele model [Eq. (2.2)] with (c1) $A_0 = 0$, (c2) $A_0 = 0.2$ and 0.4, (c3) $A_0 = 0.6$ and 0.8, (c4) $A_0 = 1$ and 1.2, (c5) $A_0 = 1.4$ and 1.6, and (c6) $A_0 = 1.8$ and 2.0. All parts of this figure use the parameters $t_1 = 1.0, \lambda_{soc} = 0.3$, and $\Omega = 10.0$. For graphs that include two values of A_0, the dashed line is based on the lower value and the solid line is based on the higher value.

transition will be focused on Fig.4.1(a),(e),(f). The transition at weak laser intensity can be easily understood. In Fig.4.1(a), increasing the laser intensity will induce the transition from topologically non-trivial states to topologically trivial states. This transition can be understood by plotting the band structure as a function of laser intensity A_0, as in Fig.4.2(a1-a6). At $A_0 = 0.0$ (laser absent), the system gap is determined by the energy difference at the $M_{1,2,3}$ points (Fig.4.2(a1)). Increasing the laser intensity tends to form a flat band in the region $M_3 - K - M_2 - K'$ (Fig.4.2(a3)). Further increasing laser intensity will set the $K(K')$ point to determine the band gap (Fig.4.2(a4)). Increasing the laser intensity still further will close, and then reopen, the gap at the K point (Fig.4.2(a5-a6)), inducing the Chern number change

TABLE 4.1: Energy gap at high symmetry point in the theoretical infinite frequency limit.

	GKM	DKM
$\mathbf{K}(\mathbf{K}')$	$6\sqrt{3}\lambda_{soc}\mathcal{J}_0(\sqrt{3}A_0)$	$2\sqrt{27\lambda_{soc}^2\mathcal{J}_0(\sqrt{3}A_0)^2+(t_1-t_d)^2\mathcal{J}_0(A_0)^2}$
$\mathbf{M}_1(\mathbf{M}_2)$	$2\left\|t_1\mathcal{J}_0(A_0)-3t_3\mathcal{J}_0(2A_0)\right\|$	$2\left\|t_d\mathcal{J}_0(A_0)\right\|$
$\mathbf{M}_3$	$2\left\|t_1\mathcal{J}_0(A_0)-3t_3\mathcal{J}_0(2A_0)\right\|$	$2\left\|(2t_1-t_d)\mathcal{J}_0(A_0)\right\|$
Γ	$6\left\|t_1\mathcal{J}_0(A_0)+t_3\mathcal{J}_0(2A_0)\right\|$	$2\left\|(2t_1+t_d)\mathcal{J}_0(A_0)\right\|$

$\Delta\mathcal{C}=\pm1$ for $K(K')$. This explains the topological transition at $A_0=1.5$. In Fig.4.1(e), the first transition at $A_0=0.4$ is induced by the three M points' band closing and reopening (Chern number change ±1 for each M point) driven by laser coupling (Fig.4.2(b2)), while the second transition at $A_0=1.5$ (Fig.4.2(b5)) is because of the $K(K')$ points closing and reopening (Chern number change ±1 for K or K' point). In Fig.4.1(f), the first transition at $A_0=0.8$ (Fig.4.2(c3)) is due to the M_3 point closing and reopening (Chern number change ±1), and the transition at $A_0=1.8$ (Fig.4.2(c6)) is due to the $K(K')$ points closing and reopening (Chern number change ±1) for K or K' point. The picture can be confirmed by plotting the Floquet band structure with different laser intensities in Fig.4.2.

4.1.2 Low energy Hamiltonian in the high frequency limit

From the Magus expansion in the high frequency regime, the effective Hamiltonian is written as

$$H_{\text{eff}}=H_0+\sum_n\frac{1}{n\Omega}[H_n,H_{-n}]+\mathcal{O}(\frac{1}{\Omega^2}), \tag{4.1}$$

where $H_{\text{eff}} = H_0$ in the theoretical infinite frequency limit. The position of the $\mathbf{K}$ point is $(4\pi/3\sqrt{3}, 0)$ (and symmetry related points), and the low-energy Hamiltonian at the high-frequency limit is given by

$$H_0 = \begin{pmatrix} 3\sqrt{3}\lambda_{soc}\mathcal{J}_0(\sqrt{3}A_0) & (t_1 - t_d)\mathcal{J}_0(A_0) \\ (t_1 - t_d)\mathcal{J}_0(A_0) & -3\sqrt{3}\lambda_{soc}\mathcal{J}_0(\sqrt{3}A_0) \end{pmatrix}. \tag{4.2}$$

For the generalized Kane-Mele model, we have $t_1 = t_d$. Then the eigenvalues will be

$$E_{\pm} = \pm 3\sqrt{3}\lambda_{soc}\mathcal{J}_0(\sqrt{3}A_0), \tag{4.3}$$

which depend on only the spin-orbit coupling λ_{soc} and scaled by Bessel function $\mathcal{J}(\sqrt{3}A_0)$. For the dimerized Kane-Mele model, the Hamiltonian is independent of the third-neighbor hopping terms t_3. The eigenvalues are

$$E_{\pm} = \pm\sqrt{27\lambda_{soc}^2\mathcal{J}_0(\sqrt{3}A_0)^2 + (t_1 - t_d)^2\mathcal{J}_0(A_0)^2}. \tag{4.4}$$

The position of $\mathbf{M}_3$ point is $(0, 2\pi/3)$, and the low-energy Hamiltonian up to second order in A_0 is given by,

$$H_0 = \begin{pmatrix} 0 & f_{\mathbf{M}_3} \\ f_{\mathbf{M}_3} & 0 \end{pmatrix}, \tag{4.5}$$

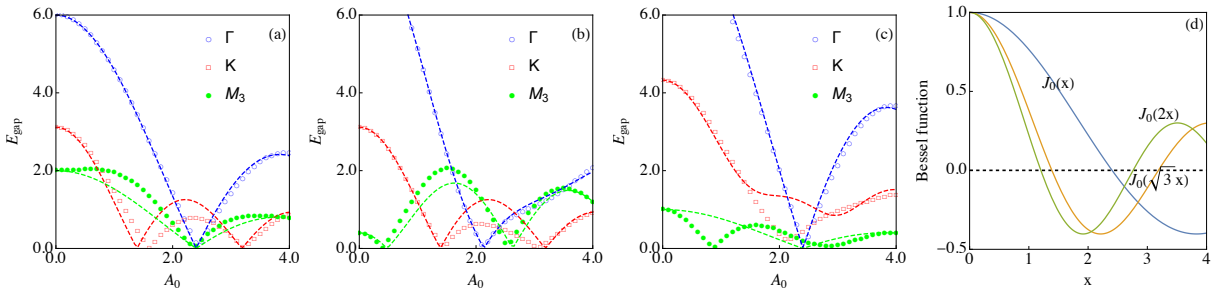

FIGURE 4.3: (Color online) The energy gaps at high symmetry points are plotted with dots. The dashed line indicates the energy gap in the theoretical infinite-frequency limit. (a) Generalized Kane-Mele model with $t_3 = 0.0$. (b) Generalized Kane-Mele model with $t_3 = 0.4$. (c) Dimerized Kane-Mele model with $t_d = 2.5$. (d) The zero-th order Bessel function of first kind used in the infinite frequency limit.

with $f_{\mathbf{M}_3} = (2t_1 - t_d)\mathcal{J}_0(A_0) - 3t_3\mathcal{J}_0(2A_0)$. The eigenvalues are

$$E_\pm = \pm\left|(2t_1 - t_d)\mathcal{J}_0(A_0) - 3t_3\mathcal{J}_0(2A_0)\right|. \tag{4.6}$$

For the generalized Kane-Mele model, we have $t_1 = t_d$, then the eigenvalues will be

$$E_\pm = \pm\left|t_1\mathcal{J}_0(A_0) - 3t_3\mathcal{J}_0(2A_0)\right|. \tag{4.7}$$

For the dimerized Kane-Mele model, the Hamiltonian is independent of third-neighbor hopping terms t_3. The eigenvalues are

$$E_\pm = \pm\left|(2t_1 - t_d)\mathcal{J}_0(A_0)\right|. \tag{4.8}$$

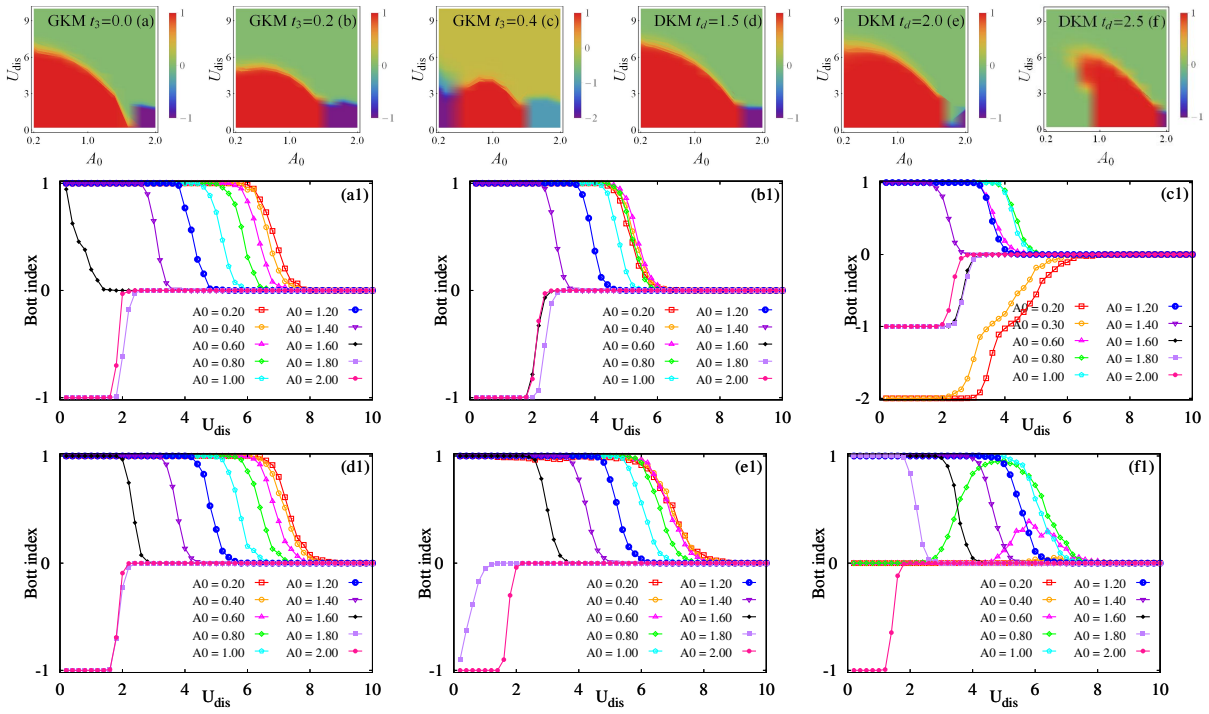

FIGURE 4.4: (Color online) Top panel: The phase diagram in the plane of laser intensity A_0 and on-site disorder U_{dis} for both GKM with $t_3 = 0.0$ (a), $t_3 = 0.2$ (b), $t_3 = 0.4$ (c) and DKM with $t_d = 1.5$ (d), $t_d = 2.0$ (e), $t_d = 2.5$ (f). Note the color scale for (c) is different from the others. The phase diagram can serve as a visual guide. The detailed data with Bott index as a function of disorder strength are plotted in the lower panels. Middle panel: Generalized Kane-Mele model with $t_3 = 0.0$ (a1), $t_3 = 0.2$ (b1), $t_3 = 0.4$ (c1) from left to right. Bottom panel: dimerized Kane-Mele model with $t_d = 1.5$ (d1), $t_d = 2.0$ (e1), $t_d = 2.5$ (f1) from left to right. The remaining model parameters are fixed at $t_1 = 1.0, \lambda_{soc} = 0.3, \Omega = 10.0$.

The position of the $\mathbf{M}_2$ point is $(-\sqrt{3}\pi/3, \pi/3)$,

$$H_0 = \begin{pmatrix} 0 & f_{\mathbf{M}_2} \\ f_{\mathbf{M}_2} & 0 \end{pmatrix}, \tag{4.9}$$

with $f_{\mathbf{M}_2} = -t_d\mathcal{J}_0(A_0) + 3t_3\mathcal{J}_0(2A_0)$. The eigenvalues are

$$E_\pm = \pm\left|-t_d\mathcal{J}_0(A_0) + 3t_3\mathcal{J}_0(2A_0)\right|. \tag{4.10}$$

For the generalized Kane-Mele model, we have $t_1 = t_d$, and the eigenvalues will be

$$E_{\pm} = \pm \left| t_1 \mathcal{J}_0(A_0) - 3t_3 \mathcal{J}_0(2A_0) \right| . \tag{4.11}$$

For the dimerized Kane-Mele model, the Hamiltonian is independent of the third-neighbor hopping terms t_3, and the eigenvalues are

$$E_{\pm} = \pm \left| t_d \mathcal{J}_0(A_0) \right| . \tag{4.12}$$

The gap for each high symmetry point in the high-frequency limit is summarized in Table 4.1. The gap size at each high symmetry $\mathbf{k}$ point is plotted with a dashed line in Fig.4.3. The exact gap size is plotted with dots, as a comparison. For the Kane-Mele model and the GKM model, the gap calculated using the high-frequency approximation can capture the main feature of the exact results, especially for the gap closing points of Γ, K, and M_3, which correspond to the spin Chern number change. For the DKM Hamiltonian, the high frequency results are in good agreement for the Γ point. Higher order corrections are needed to explain the gap closing point around $A_0 = 0.8$ for the M_3 points and the minimum at around $A_0 = 2.2$ for the K point.

4.2 Phase diagram and Bott index for the disordered system

In the top panels of Fig.4.4(a-d), we plot the phase diagram of the GKM model with parameter $t_3 = 0.0, 0.2, 0.4$ and the DKM model with $t_d = 1.5, 2.0, 2.5$. The remaining parameters are fixed at $t_1 = 1.0, \lambda_{soc} = -0.3, \Omega = 10.0$. The detailed data corresponding to the phase

diagram–the Bott index as a function of disorder at different laser intensities–are plotted in the middle panels for GKM with $t_3 = 0.0, 0.2, 0.4$ from left to right and the bottom panels for DKM with $t_d = 1.5, 2.0, 2.5$. In the clean system limit ($U_{dis} = 0$), the system makes a topological transition as the laser intensity increases, inducing the Dirac points to close and reopen (shown in Fig.4.2). The inclusion of disorder in the weak disorder region does not change the original states from topological trivial or non-trivial. In the strong disorder limit, a topologically trivial (Bott index=0) Anderson insulator appears.

The most interesting phenomena occur for intermediate levels of disorder. Consider Fig.4.4 (a), (c), and (f), which represents the Kane-Mele model, the GKM, and the DKM, respectively. Reading the figures horizontally, for fixed disorder strength, as the laser intensity increases, the transition from the topologically non-trivial state to the topologically trivial state occurs in Fig.4.4(a). These results are not easy to explain because the band structure at the starting point with finite disorder strength is not well-defined (momentum is not a good quantum number). As an alternative, one can read the figure vertically, for fixed laser intensity, and study the effect of disorder on the the original Floquet Bloch states. In this way, the starting point is the Floquet-Bloch band structure shown in Fig.4.2 in the first Floquet zone $-\Omega/2 < E_{\mathbf{k}} < \Omega/2$.

Let us focus on Fig.4.4(a) and Fig.4.4(a1) first. We define the critical disorder strength as the point where the Bott index deviates from 1. A monotonic behavior is observed for $A_0 = 0.2, 0.4, \cdots 1.6$. By inspecting the Floquet band structure for $A_0 = 0.2, 0.4, 0.6, 0.8$ [Fig.4.2(a2-a3)], one realizes the band gap at the M point does not change much while the band width is narrowing. This observation explains the results here because for weak laser intensity, the hopping terms are renormalized by a Bessel function $J_n(x) < 1$, while the on-site

disorder term remains unchanged. Thus, critical disorder will decrease at weak laser intensity. Further increasing $A_0 = 1.0, 1.2, 1.4, 1.6$ [Fig.4.2(a4-a5)], the Floquet-Bloch band structure is significantly changed (the system gap shifts to the K point). In this process, both the bandwidth and system gap decrease, which decreases the critical disorder strength faster. Finally, at laser intensity $A_0 = 1.8, 2.0$ [Fig.4.2(a6)], the bandwidth decreases dramatically while the system gap starts to increase, and the competition between them determines the critical disorder strength.

Next, we turn to the Bott index as a function of disorder for the generalized Kane-Mele model with $t_3 = 0.4$, shown in Fig.4.4(c1). First we consider low laser intensity: $A_0 = 0.2, 0.3$. As the laser intensity is increased from $A_0 = 0.2$ to $A_0 = 0.3$, both the bandwidth and the gap at the M point get smaller, which explains why the critical U_{dis} decreases. Around $A_0 = 0.4$, the system gap at the M point closes and reopens. Further increasing the laser intensity to $A_0 = 0.6, 0.8$ will increase the gap at the M point, which pushes the critical U_{dis} to larger values. Further increasing A_0 to 1.0 and 1.2, the system gap shifts to the K point (shown in Fig.4.2(b5)); this pushes the critical disorder to smaller values. The system gap at the K point closes and reopens at $A_0 = 1.4$. Finally, the minimal gap shifts to the Γ point, and further decreases as the laser intensity increases to $A_0 = 2.0$, which explains the critical disorder strength moving to smaller values from $A_0 = 1.8$ to $A_0 = 2.0$.

Finally, by looking at the data for the dimerized KM model in Fig.4.4(f1), we find a similar story, except differing for $A_0 < 0.8$. We focus our discussion on this region. The starting point here is the topological trivial state with spin Chern number $\mathcal{C} = 0$. For weak laser intensity $A_0 = 0.2, 0.4$, adding disorder does not change the Bott index. The gap is relative large here,

and neither weak nor intermediate disorder can close the gap and generate band inversion. Strong disorder, however, will localize all the states. This idea is confirmed by inspecting the data for $A_0 = 0.6, 0.8$. Here the gap at the M_3 point gets smaller, and the intermediate disorder strength will close the gap and reopen it, which can be explained by the Born approximation, where the mass is renormalized through disorder. We find the highest values of the data for $A_0 = 0.6, 0.8$ do not reach 1, which would indicate a topologically non-trivial state. This is explained as a finite size effect because larger system sizes move the Bott index towards 1; more detail is provided as an appendix.

4.3 Phase diagram and Bott index for disordered system with an on-resonant laser

In this section, we study the topological invariant as a function of laser intensity and on-site disorder while fixing the laser frequency to be on-resonant ($\hbar\Omega < W$, where W is the bandwidth of equilibrium model Hamiltonian). In the on-resonant regime, the high-frequency expansion is not expected to be accurate and the system may display a complex evolution as a function of laser parameters.

In the top panels of Fig.4.5, we plot the Chern number as a function of on-site disorder U_{dis} for (a) GKM model with $t_3 = 0.0$ (bandwidth $6t_1$), (b) GKM model with $t_3 = 0.2$ (bandwidth $7.2t_1$) and (c) DKM model with $t_d = 1.5$ (bandwidth $7.0t_1$). The remaining model parameters are fixed at $t_1 = 1.0, \lambda_{soc} = 0.3, \Omega = 5.0$. The laser intensity is varied through

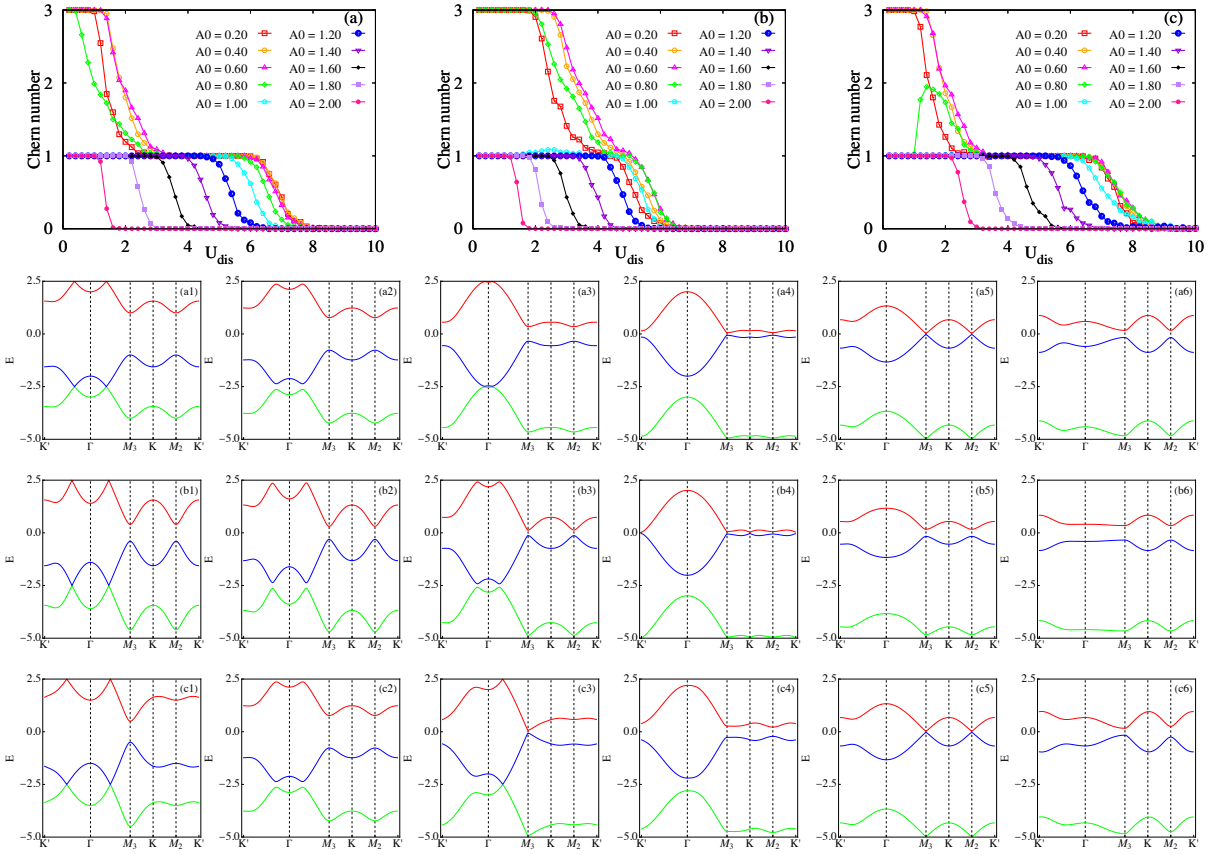

FIGURE 4.5: (Color online) The Chern number as a function of on-site disorder U_{dis} for (a) GKM model with $t_3 = 0.0$, (b) GKM model with $t_3 = 0.2$ (c) DKM model with $t_d = 1.5$. The remaining model parameters are fixed at with $t_1 = 1.0, \lambda_{soc} = 0.3, \Omega = 5.0$. The Floquet-Bloch band structure in the clean-limit (absence of disorder) are plotted for different laser intensity $A_0 = 0.0, 0.4, 0.8, 1.2, 1.6, 2.0$ in (a1-a6) for GKM model with $t_3 = 0.0$, (b1-b6) for GKM model with $t_3 = 0.2$ and (c1-c6) for DKM model with $t_d = 1.5$.

$A_0 = 0.2, 0.4, 0.6, \cdots, 2.0$. We focus on the clean limit first, increasing the laser intensity from $A_0 = 0.2$ to $A_0 = 2.0$, and note the Chern number will change from $\mathcal{C} = 3$ to $\mathcal{C} = 1$ which is $\Delta\mathcal{C} = 2$. This behavior can be understood by considering the decrease of the laser frequency from infinity to finite on-resonant frequency: At infinite laser frequency, the original equilibrium bandwidth is rescaled by a Bessel function of the first kind. For example, the effective bandwidths W_{eff} are $6|\mathcal{J}_0(A_0)t_1|$ for the Kane-Mele model, $6|\mathcal{J}_0(A_0)t_1 + 2\mathcal{J}_0(2A_0)t_3|$ for the GKM model and $2|\mathcal{J}(A_0)(t_d + 2t_1)|$ for the DKM model. The next order correction in the

high-frequency limit is a correction to this effective bandwidth. When the laser frequency is decreased to be equal to the effective bandwidth, the "top" of a "lower" Floquet copy will touch the "bottom" of the "upper" Floquet band at $E = -\Omega/2$. Further decreasing the frequency will generate a quadratic band crossing and a small but finite laser intensity will open a gap between the band crossing, changing the Chern number by $\Delta\mathcal{C} = \pm 2$.

To further illustrate the picture above, the Floquet-Bloch band structure in the clean-limit (absence of disorder) is plotted for different laser intensities $A_0 = 0.0, 0.4, 0.8, 1.2, 1.6, 2.0$ in (a1-a6) for the KM model with $t_3 = 0.0$, (b1-b6) for the GKM model with $t_3 = 0.2$ and (c1-c6) for the DKM model with $t_d = 1.5$. The quasi-energy bands are plotted from $-\Omega$ to $\Omega/2$ which includes the copy in the Floquet zone $-\Omega/2 < \epsilon < \Omega/2$ and half of the lower copy $-\Omega < \epsilon < -\Omega/2$ to show the band crossing point at Γ. We focus on the behavior of the Chern number with the laser intensity $A_0 = 0.8$. In the KM model, the Floquet-Bloch band structure is shown in Fig.4.5(a3). The system gap is situated very close to the Γ point and is small compared to the system gap at the M_3 point. In this way, a small amount of disorder will close the gap around the $|\Gamma|$ point first (changing the Chern number by 2), and then close the gap at the M_3 point, changing the Chern number by 1. The magnitude $\mathcal{C} = 1$ is the result of the gap differences at energy $E = -\Omega/2$ and $E = 0.0$. This picture is confirmed by comparing the data for the GKM model with $t_3 = 0.2$ [shown in Fig.4.5(b) and (b3)]. Since the original bandwidth of the model is larger than the bandwidth of KM model, the gap formed at $E = -\Omega/2$ is larger. This may generate the larger critical disorder to change the Chern number by ± 2. Secondly, the energy gap difference at energy at $E = -\Omega/2$ and $E = 0.0$ is relatively smaller, which induces the smaller magnitude of $\mathcal{C} = 1$.

For the DKM model with $A_0 = 0.8$, the Chern number changes from 1 to 2 with small disorder strength and comes back to 1 as the disorder increases. By inspecting the Floquet-Bloch band structure in Fig.4.5(c3), we realize there is a linear crossing between the Γ and M_3 points. A small amount of disorder can induce an effective mass which generates a band inversion and a Chern number change ± 1. Further increasing the intensity will close the gap and bring one back to $\mathcal{C} = 1$. Continuing to increase the disorder will induce the transition from 1 to 0, which is determined by the energy gap at $E = 0.0$.

4.4 Conclusion

In this thesis we theoretically studied the topological properties of the generalized Kane-Mele (GKM) model with third-neighbor hopping t_3 and the dimerized Kane-Mele (DKM) model with dimerized hopping t_d along the vertical direction [along δ_3 in Fig.2.1(a)] under illumination by a circularly polarized monochromatic laser field. In the absence of the laser, the GKM model has a critical value of $t_3 = 1/3$, where topological trivial and non-trivial states occur for values larger and smaller than the critical t_3, respectively. The DKM model has critical $t_d = 2.0$ where topological trivial and non-trivial states occur for values larger and smaller than the critical t_d, respectively.

To include both topologically trivial and non-trivial states as starting points, we chose $t_3 = 0.0, 0.2, 0.4$ for the GKM model and $t_d = 1.5, 2.0, 2.5$ for the DKM model. Their complicated phase structures were studied numerically, both in the high-frequency off-resonant case and

the low-frequency resonant case. The topological transitions are explained using the Floquet-Bloch band structure, where we find the laser will close and reopen Dirac points, inducing a Chern number change $\Delta\mathcal{C} = \pm 1$ for each Dirac point. Further, we found the laser can shift the system gap between different high symmetry points. For example, the minimal gap may shift from an M point to a K point in the Kane-Mele model [shown in Fig.4.2(a1-a6)] or even shift to some point without high symmetry for the DKM model [shown in Fig.4.2(c1-c6)]. The band structure, and the system gap at high symmetry points, is explained using the low-energy Hamiltonian based on a high frequency expansion for the off-resonant case.

Finally, we study the effect of on-site disorder in the GKM and DKM model under a periodic laser drive (Floquet system). Topological states are sustained with weak disorder, and destroyed by strong disorder, similar to the case in equilibrium. In addition, weak disorder may even generate a topologically trivial state from a non-trivial one providing a level of material control through the interplay of disorder and a periodic drive. Compared to the more heavily studied Kane-Mele model with disorder, the minimal gap evolution through the Brillouin zone for the GKM and DKM models presents new phenomenology for disordered Floquet systems.

Appendix: Finite size effect

The finite size effect on the non-quantized region of the Bott index where the Floquet-Anderson topological transition occurs is studied here. In Fig.4.4(c1) there exists a plateau around the Bott index 1 with $A_0 = 0.2, 0.3$ and (f1) the Bott index does not reach 1 with $A_0 = 0.6, 0.8$. Here we studied the two cases with different size to check what the finite size effect is.

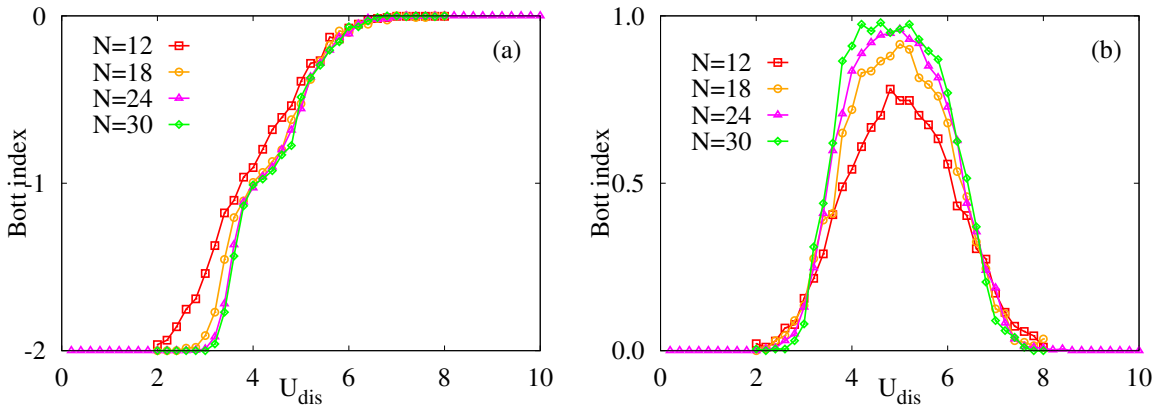

FIGURE 4.6: (Color online) (a) The Bott index as a function of on-site disorder U_{dis} for the GKM with $t_3 = 0.4$ and laser intensity $A_0 = 0.2$. (b) The Bott index as a function of on-site disorder U_{dis} for the DKM model with $t_d = 2.5$ and laser intensity $A_0 = 0.8$. The remaining model parameters are fixed at $t_1 = 1.0, \lambda_{soc} = 0.3, \Omega = 10.0$. Different cluster sizes are chosen to illustrate the finite size effect. The total number of lattice sites are $N \times N \times 2$ where the 2 comes from the number of atoms in one unit cell.

In Fig.4.6, we plot the disorder- averaged Bott index as a function of disorder for different system sizes. It is clear that with increasing system size, the non-quantized region of the Bott index becomes sharper, which is consistent with previous studies.[55, 57] Further, in Fig.4.6(b), we realize there will be a quantized area with increasing cluster size.

Acknowledgements

We acknowledge helpful discussions with Hsiang-Hsuan Hung, Yang Ge, Quansheng Wu, and Yingyue Boretz. We gratefully acknowledge funding from Army Research Office Grant No. W911NF-14-1-0579, NSF Grant No. DMR-1507621, and NSF Materials Research Science and Engineering Center Grant No. DMR-1720595. GAF gratefully acknowledges support from the Simons Foundation Fellows program.

5

Conclusion

This thesis examined, with theory and computation, the topological properties of several extensions of the Kane-Mele model. These were the generalized Kane-Mele model, with third-nearest neighbor hopping, and the dimerized Kane-Mele model, in which the first-nearest neighbor hopping strength is different for bonds parallel to the y-axis.

The effects were studied of a circularly polarized monochromatic laser illuminating the system and of on-site disorder. Phase diagrams were produced to show the topologically trivial and non-trivial phases of the system.

Finding topologically insulating phases may open the door to practical uses in the future. Examples include optoelectronics and energy efficient computer memory via spintronics.

The systems simulated in this thesis display phases in which they are topological insulators and trivial insulators, and it is possible to switch between those phases by adjusting the values

of the parameters. One possible application of this is to detect the influence of a laser. If the system is in a trivial phase and then suddenly switches to having conducting surface states characteristic of a topological insulator, then the laser is detected. Laser controlled conductivity allows for a variety of applications in, for example, optoelectronics.

In a topological insulator, the spin of the electrons in the metallic surface states is tied to their momentum. In order to stop moving around the edge of the material, an electron would have to change its energy or spin state (electrons going the opposite direction have opposite spin), which limits ways in which electrons can scatter. The result is less dissipation of currents in the conducting surface states than would be expected from a bulk metal.

If electrons with spins that point one way more than the opposite way are conducted into a thin layer of ferromagnetic material, the spins of the incoming electrons can interact with the spins of the existing electrons, so the spins in the ferromagnet may be changed to match. This can change the direction of magnetization in the ferromagnet. The direction of magnetization of the ferromagnet can be used to encode the value of a bit of computer memory. By passing electric current though the metallic surface states of a topological insulator and into a thin layer of ferromagnet, bits can be read or rewritten. Using a topological insulator to polarize the spins of the electrons could potentially work with far lower currents than the existing method, which uses a thick ferromagnetic layer to create the spin polarization. Less current and lower dissipation mean less heat generated, which mitigates a major issue faced by the densely packed circuits found in modern computing devices. Such circuits would be considered spintronic because they rely on the spin of the electrons, not just their charge.

Bibliography

[1] J. E. Moore, Nature **464**, 194 (2010).

[2] M. Z. Hasan, and C. L. Kane, Rev. Mod. Phys. **82**, 3045 (2010).

[3] X.-L. Qi, and S.-C. Zhang, Rev. Mod. Phys. **83**, 1057 (2011).

[4] Y. Ando, J. Phys. Soc. Japan **82**, 102001 (2013).

[5] J. Maciejko, and G. A. Fiete, Nat. Phys. **11**, 385 (2015).

[6] A. Stern, Annu. Rev. Condens. Matter Phys. **7**, 349 (2016).

[7] W. Witczak-Krempa, G. Chen, Y. B. Kim, and L. Balents, Annual Review of Condensed Matter Physics **5**, 57 (2014).

[8] A. Mesaros, and Y. Ran, Phys. Rev. B **87**, 155115 (2013).

[9] X. Chen, Z.-C. Gu, Z.-X. Liu, and X.-G. Wen, Phys. Rev. B **87**, 155114 (2013).

[10] K. Sun, H. Yao, E. Fradkin, and S. A. Kivelson, Phys. Rev. Lett. **103**, 046811 (2009).

[11] F. Xue, and X.-X. Zhang, Phys. Rev. B **96**, 195160 (2017).

[12] F. Xue, and A. H. MacDonald, Phys. Rev. Lett. **120**, 186802 (2018).

[13] Z. Y. Meng, T. C. Lang, S. Wessel, F. F. Assaad, and A. Muramatsu, Nature **464**, 847 (2010).

[14] M. Hohenadler, T. C. Lang, and F. F. Assaad, Phys. Rev. Lett. **106**, 100403 (2011).

[15] S.-L. Yu, X. C. Xie, and J.-X. Li, Phys. Rev. Lett. **107**, 010401 (2011).

[16] Y.-F. Wang, Z.-C. Gu, C.-D. Gong, and D. N. Sheng, Phys. Rev. Lett. **107**, 146803 (2011).

[17] N. H. Lindner, G. Refael, and V. Galitski, Nat. Phys. **7**, 490 (2011).

[18] G. Jotzu, M. Messer, R. Desbuquois, M. Lebrat, T. Uehlinger, D. Greif, and T. Esslinger, Nature **515**, 237 (2014).

[19] T. Bilitewski, and N. R. Cooper, Phys. Rev. A **91**, 063611 (2015).

[20] T. Oka, and H. Aoki, Phys. Rev. B **79**, 081406 (2009).

[21] T. Kitagawa, E. Berg, M. Rudner, and E. Demler, Phys. Rev. B **82**, 235114 (2010).

[22] B. M. Fregoso, Y. H. Wang, N. Gedik, and V. Galitski, Phys. Rev. B **88**, 155129 (2013).

[23] M. Sentef, M. Claassen, A. Kemper, B. Moritz, T. Oka, J. Freericks, and T. Devereaux, Nat. Commun. **6**, 7047 (2015).

[24] Y. H. Wang, H. Steinberg, P. Jarillo-Herrero, and N. Gedik, Science **342**, 453 (2013).

[25] F. Mahmood, C.-K. Chan, Z. Alpichshev, D. Gardner, Y. Lee, P. A. Lee, and N. Gedik, Nat. Phys. **12**, 306 (2016).

[26] H. L. Calvo, L. E. F. Foa Torres, P. M. Perez-Piskunow, C. A. Balseiro, and G. Usaj, Phys. Rev. B **91**, 241404 (2015).

[27] V. Dal Lago, M. Atala, and L. E. F. Foa Torres, Phys. Rev. A **92**, 023624 (2015).

[28] P. M. Perez-Piskunow, L. E. F. Foa Torres, and G. Usaj, Phys. Rev. A **91**, 043625 (2015).

[29] P. M. Perez-Piskunow, G. Usaj, C. A. Balseiro, and L. E. F. F. Torres, Phys. Rev. B **89**, 121401 (2014).

[30] H. Dehghani, T. Oka, and A. Mitra, Phys. Rev. B **90**, 195429 (2014).

[31] H. Dehghani, T. Oka, and A. Mitra, Phys. Rev. B **91**, 155422 (2015).

[32] L. D'Alessio, and M. Rigol, Nat. Commun. **6**, 8336 (2015).

[33] V. E. Sacksteder, and Q. Wu, Phys. Rev. B **94**, 205424 (2016).

[34] L. Du, X. Zhou, and G. A. Fiete, Phys. Rev. B **95**, 035136 (2017).

[35] L. Du, and G. A. Fiete, Phys. Rev. B **95**, 235309 (2017).

[36] Y. Ge, and M. Rigol, Phys. Rev. A **96**, 023610 (2017).

[37] Q. Chen, L. Du, and G. A. Fiete, Phys. Rev. B **97**, 035422 (2018).

[38] M. Ezawa, Phys. Rev. Lett. **110**, 026603 (2013).

[39] M. Finazzi, M. Savoini, A. R. Khorsand, A. Tsukamoto, A. Itoh, L. Duò, A. Kirilyuk, T. Rasing, and M. Ezawa, Phys. Rev. Lett. **110**, 177205 (2013).

[40] J. Li, R.-L. Chu, J. K. Jain, and S.-Q. Shen, Phys. Rev. Lett. **102**, 136806 (2009).

[41] C. W. Groth, M. Wimmer, A. R. Akhmerov, J. Tworzydło, and C. W. J. Beenakker, Phys. Rev. Lett. **103**, 196805 (2009).

[42] H. Jiang, L. Wang, Q.-f. Sun, and X. C. Xie, Phys. Rev. B **80**, 165316 (2009).

[43] H. Jiang, S. Cheng, Q.-f. Sun, and X. C. Xie, Phys. Rev. Lett. **103**, 036803 (2009).

[44] E. Prodan, T. L. Hughes, and B. A. Bernevig, Phys. Rev. Lett. **105**, 115501 (2010).

[45] V. Chua, and G. A. Fiete, Phys. Rev. B **84**, 195129 (2011).

[46] D. Xu, J. Qi, J. Liu, V. Sacksteder, X. C. Xie, and H. Jiang, Phys. Rev. B **85**, 195140 (2012).

[47] Q. Wu, L. Du, and V. E. Sacksteder, Phys. Rev. B **88**, 045429 (2013).

[48] J. Song, and E. Prodan, Phys. Rev. B **89**, 224203 (2014).

[49] J. Song, C. Fine, and E. Prodan, Phys. Rev. B **90**, 184201 (2014).

[50] A. Girschik, F. Libisch, and S. Rotter, Phys. Rev. B **91**, 214204 (2015).

[51] C. P. Orth, T. Sekera, C. Bruder, and T. L. Schmidt, Sci. Rep. **6**, 24007 (2016).

[52] J. Song, H. Liu, H. Jiang, Q.-f. Sun, and X. C. Xie, Phys. Rev. B **85**, 195125 (2012).

[53] C. L. Kane, and E. J. Mele, Phys. Rev. Lett. **95**, 146802 (2005).

[54] C. L. Kane, and E. J. Mele, Phys. Rev. Lett. **95**, 226801 (2005).

[55] H.-H. Hung, A. Barr, E. Prodan, and G. A. Fiete, Phys. Rev. B **94**, 235132 (2016).

[56] T. A. Loring, and M. B. Hastings, EPL (Europhysics Lett. **92**, 67004 (2010).

[57] P. Titum, N. H. Lindner, M. C. Rechtsman, and G. Refael, Phys. Rev. Lett. **114**, 056801 (2015).

[58] P. Titum, E. Berg, M. S. Rudner, G. Refael, and N. H. Lindner, Phys. Rev. X **6**, 021013 (2016).

[59] T. Fukui, Y. Hatsugai, and H. Suzuki, Journal of the Physical Society of Japan **74**, 1674 (2005).